

# Li Intercalation in MoS<sub>2</sub>: In Situ Observation of Its Dynamics and Tuning Optical and Electrical Properties

Feng Xiong,<sup>†,‡</sup> Haotian Wang,<sup>§</sup> Xiaoge Liu,<sup>||</sup> Jie Sun,<sup>‡</sup> Mark Brongersma,<sup>||</sup> Eric Pop,<sup>\*,†</sup> and Yi Cui<sup>\*,‡,||,⊥</sup>

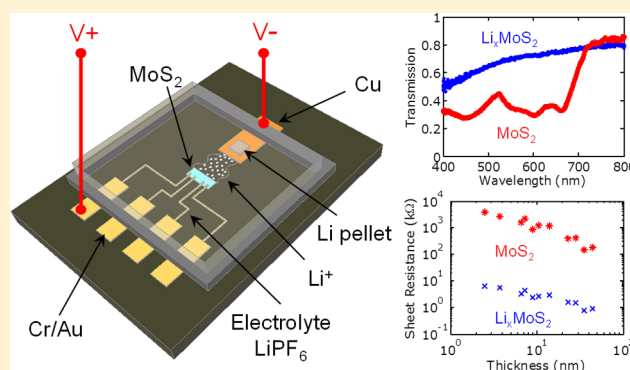
<sup>†</sup>Department of Electrical Engineering, <sup>‡</sup>Department of Materials Science and Engineering, <sup>§</sup>Department of Applied Physics, and <sup>||</sup>Geballe Laboratory for Advanced Materials, Stanford University, Stanford, California 94305, United States

<sup>⊥</sup>Stanford Institute for Materials and Energy Sciences, SLAC National Accelerator Laboratory, 2575 Sand Hill Road, Menlo Park, California 94025, United States

## Supporting Information

**ABSTRACT:** Two-dimensional layered materials like MoS<sub>2</sub> have shown promise for nanoelectronics and energy storage, both as monolayers and as bulk van der Waals crystals with tunable properties. Here we present a platform to tune the physical and chemical properties of nanoscale MoS<sub>2</sub> by electrochemically inserting a foreign species (Li<sup>+</sup> ions) into their interlayer spacing. We discover **substantial enhancement of light transmission (up to 90% in 4 nm thick lithiated MoS<sub>2</sub>) and electrical conductivity (more than 200×) in ultrathin (~2–50 nm) MoS<sub>2</sub> nanosheets after Li intercalation due to changes in band structure that reduce absorption upon intercalation and the injection of large amounts of free carriers.** We also capture the first in situ optical observations of Li intercalation in MoS<sub>2</sub> nanosheets, shedding light on the dynamics of the intercalation process and the associated spatial inhomogeneity and cycling-induced structural defects.

**KEYWORDS:** MoS<sub>2</sub>, intercalation, lithiation, in situ, electrochemical



Molybdenum disulfide (MoS<sub>2</sub>) is a member of a family of two-dimensional (2D) layered transition metal dichalcogenides (TMDs).<sup>1</sup> Because of their unique combinations of physical and chemical properties,<sup>2–4</sup> as well as their 2D nature (the ability to be thinned down to monolayer), TMDs have attracted research interest in areas of nanoelectronics,<sup>5</sup> optoelectronics,<sup>6</sup> energy storage devices,<sup>7</sup> thermoelectric devices,<sup>8</sup> flexible electronics,<sup>9</sup> and electrocatalysis.<sup>10</sup> The large interlayer separation in MoS<sub>2</sub> (~0.65 nm) provides perfect locations to accommodate guest species such as alkali metal ions (Li<sup>+</sup>, Na<sup>+</sup>, and K<sup>+</sup>) through a process known as intercalation. Intercalation in layer-structured materials such as graphite and MoS<sub>2</sub> have been extensively studied for applications in energy storage,<sup>11</sup> liquid phase exfoliation,<sup>12</sup> and electrocatalysis.<sup>13,14</sup> It has been reported that intercalation causes changes in the host materials' electronic structure,<sup>15–17</sup> resulting in considerable variation in their optical and electrical properties.<sup>18–21</sup> Similarly, intercalation in Li<sub>x</sub>CoO<sub>2</sub> has demonstrated tunable thermal conductivity through intercalation-dependent phase behavior and phonon scattering.<sup>22</sup> Large quantity of zerovalent metal intercalation has also been developed recently.<sup>20,23,24</sup>

In this study, we develop a novel platform to electrochemically intercalate Li atoms into the interlayer spacing of ultrathin MoS<sub>2</sub> nanosheets, controllably tuning the physical and chemical properties of the material. Our electrochemical device allows in

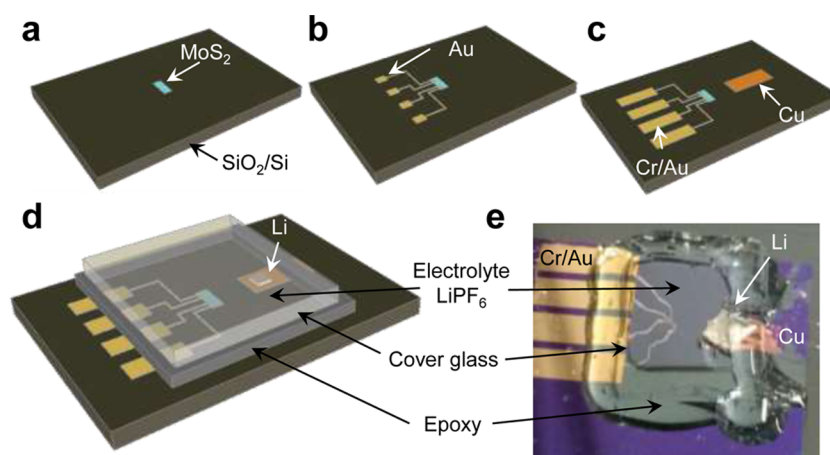
situ characterization of both optical and electrical properties during the lithiation/delithiation process. While previous work<sup>19</sup> focused on the effect of lithiation in MoS<sub>2</sub> for energy storage applications by irreversibly converting MoS<sub>2</sub> to Li<sub>2</sub>S, our study emphasizes controllably and reversibly tuning the physical properties of MoS<sub>2</sub> films by varying Li concentration in interlayer gaps. Our work also captures the first set of in situ observations of the dynamics of the Li intercalation process in MoS<sub>2</sub> nanosheets. Through Raman measurement and band structure calculations, we provide possible explanations for the simultaneous enhancement of optical transmission and electrical conductivity upon lithiation, providing a path to dynamically tune the physical properties of such layered materials.

Figure 1 illustrates the sample fabrication process of our electrochemical platform, which allows us to characterize the optical and electrical properties of MoS<sub>2</sub> while we perform Li intercalation. We first mechanically exfoliated ultrathin MoS<sub>2</sub> nanosheets (~2–50 nm) onto SiO<sub>2</sub>/Si substrates (Figure 1a). The MoS<sub>2</sub> thickness was determined by atomic force microscopy (AFM). We then put down metal electrodes via electron-beam (e-beam) lithography and shadow mask

Received: July 2, 2015

Revised: August 28, 2015

Published: September 9, 2015



**Figure 1.** Schematics. (a–d) Schematics of the fabrication process of nanoscale  $\text{MoS}_2$  device for in situ Li intercalation. (e) Optical image of an as-fabricated device. See [Methods](#) for more details of the fabrication procedures. The thin Au lines appear intentionally “wavy” in the fabricated sample to avoid contacting other bulky  $\text{MoS}_2$  flakes (from the exfoliation step) that are present on the substrate.

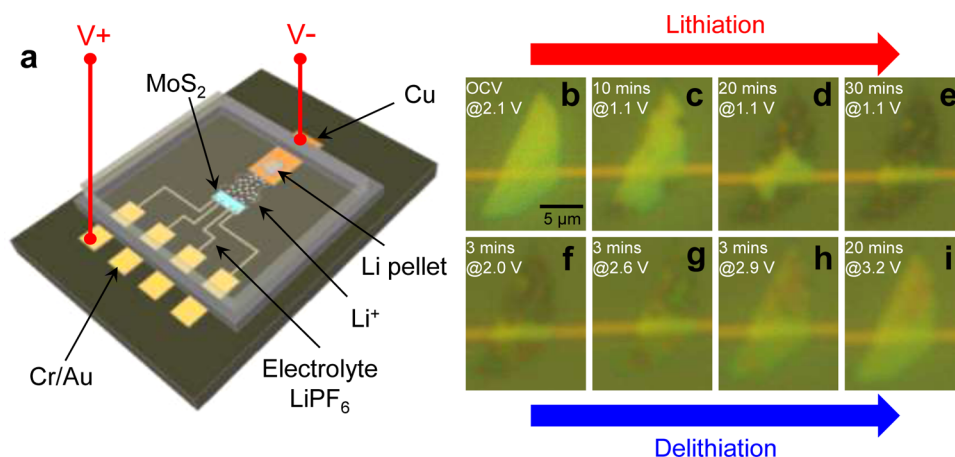


**Figure 2.** Direct observations of the dynamics of lithiation and delithiation process in  $\text{MoS}_2$ . (a) Experimental setup for electrochemical tuning of Li concentration in  $\text{MoS}_2$ . (b–e) Optical images of a thin ( $\sim 20$ – $35$  nm)  $\text{MoS}_2$  flake during the lithiation process. Initially, the flake had an open circuit voltage (OCV) of  $2.1$  V versus  $\text{Li}/\text{Li}^+$ . When holding at voltages of  $1.2$  V or higher versus  $\text{Li}/\text{Li}^+$ , no visible changes were observed even after extended periods of time. While holding at  $1.1$  V versus  $\text{Li}/\text{Li}^+$ , we observed that significant amount of  $\text{Li}^+$  ions were intercalated into  $\text{MoS}_2$  flake from the edges and  $\text{MoS}_2$  underwent a  $2\text{H}$  to  $1\text{T}$  phase transformation. These were evident from the dark spots in the flake. (f–i) Optical images of the same flake during the delithiation process. Reversible delithiation was achieved by biasing  $\text{MoS}_2$  flake at higher voltages versus  $\text{Li}/\text{Li}^+$ . As the voltage was increased,  $\text{Li}^+$  ions moved out of the flake from the edges. At  $3.2$  V versus  $\text{Li}/\text{Li}^+$ , the  $\text{MoS}_2$  flake almost went back to its original color. The top of the flake in (f) appeared to be red instead of yellow (originally), which indicated a slightly increased thickness. This is probably due to the structural change in  $\text{MoS}_2$  upon Li intercalation.

evaporation as shown in [Figure 1b,c](#) (see [Methods](#) for more details). To perform electrochemical intercalation, we adopted a planar nanobattery configuration ([Figure 1d](#)) where Li metal and  $\text{MoS}_2$  nanosheets were used as counter and working electrodes, respectively. The device with electrolyte ( $1$  M  $\text{LiPF}_6$  in  $1:1$  w/w ethylene carbonate/diethyl carbonate from EMD Chemicals) was sandwiched by the top glass slide and bottom substrate and sealed with epoxy to prevent oxidation ([Figure 1e](#)). This platform allows us to carry out Li intercalation and at the same time characterize the optical and electrical properties of  $\text{MoS}_2$  in situ. The electrochemical intercalation was performed using a SP-150 BioLogic workstation (see [Methods](#)).

With a transparent glass slide as the top seal, our electrochemical cell serves as an excellent platform to study the dynamics of Li intercalation in nanoscale  $\text{MoS}_2$  flake. A freshly packaged  $\text{MoS}_2$  nanosheet typically shows an open circuit voltage (OCV) between  $1.8$  and  $2.2$  V with respect to

$\text{Li}/\text{Li}^+$ . We carried out Li intercalation by gradually lowering the  $\text{MoS}_2$  potential with respect to  $\text{Li}/\text{Li}^+$  from  $2.0$  to  $1.0$  V with steps of  $0.1$  V or less ([Figure 2a](#)). We avoided going below  $1.0$  V versus  $\text{Li}/\text{Li}^+$  to prevent any irreversible conversion reaction that forms  $\text{Li}_2\text{S}$ .<sup>7,25</sup> [Figure 2b–i](#) depicts the first Li intercalation cycle for a typical  $\text{MoS}_2$  nanosheet. We measured the thickness of this flake ([Figure 2b](#)) by AFM, which was  $\sim 23$  nm at the bottom (green region) and  $\sim 32$  nm at the top (yellow region). When we gradually lithiated this  $\text{MoS}_2$  nanosheet by driving down its potential with respect to Li from  $2.1$  V (as packaged) to  $1.2$  V in steps of  $0.1$  V, we observed no significant change in the morphology and color of the flake under the optical microscope, even under extended stress time ( $40$  min at  $1.2$  V versus  $\text{Li}/\text{Li}^+$ , see [Supporting Information Figure 2](#)).

When we further lowered the  $\text{MoS}_2$  potential to  $1.1$  V with respect to Li, we started to visualize the Li intercalation process under optical microscope. [Figure 2c](#) illustrates that  $\text{MoS}_2$

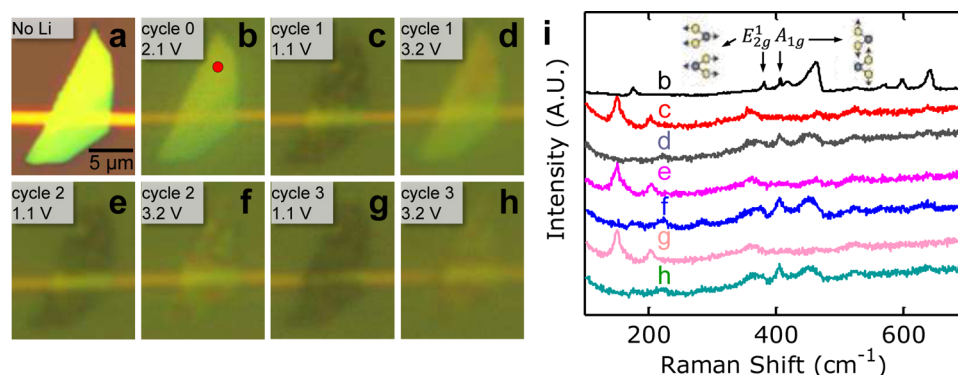


**Figure 3.** Cycling effects on MoS<sub>2</sub> nanosheet and Raman spectroscopy. (a–h) Optical reflection images of the same MoS<sub>2</sub> flake in Figure 2 at different cycles of Li intercalations. MoS<sub>2</sub> nanosheet showed progressively more structural defects as we repeatedly lithiate/delithiate the flake. These were evident from the nonuniform color change (green/yellow to red) across the flake, possibly due to an increase in interlayer thickness from Li intercalation dependent volume expansion. (i) Raman spectroscopy of the MoS<sub>2</sub> flake at different cycles, corresponding to (b–h) as indicated in the diagram. The red dot in (b) indicates the location of the Raman scan. The locations of first order phonon modes E<sub>2g</sub><sup>1</sup> (382 cm<sup>-1</sup>) and A<sub>1g</sub> (408 cm<sup>-1</sup>) are labeled in graph. The inset shows the corresponding phonon vibration mode. After the first cycle, all Raman spectra (c–h) showed a broadening of line width of E<sub>2g</sub> mode, which usually indicates high impurity scattering and structural defects. Whenever the flake is fully lithiated (c,e,g), A<sub>1g</sub> peak intensity decreased significantly, suggesting the dissociation of interlayer bonding due to influx of Li<sup>+</sup> ions. At the same time, peaks at ~150 and 200 cm<sup>-1</sup> started to appear, possibly due to a 2H to 1T phase transformation in MoS<sub>2</sub>. When the flake was delithiated (b,d,f,h), A<sub>1g</sub> mode reappears as interlayer bonding was restored.

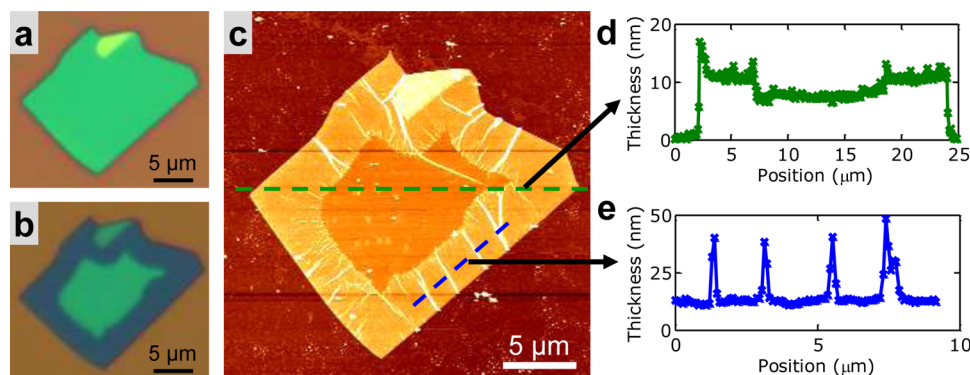


**Figure 4.** Strain in MoS<sub>2</sub> nanosheet after Li intercalation. (a,b) Optical images of a MoS<sub>2</sub> nanosheet before and after 2 h of chemical Li intercalation. The outer ring in (b) indicates that Li ions enter MoS<sub>2</sub> from the edges. The scale bars are 5 μm. (c) AFM image of the same MoS<sub>2</sub> nanosheet in (b) after 2 h of Li intercalation. The lithiated region showed a significant increase in thickness (~50%) due to the incoming Li ions. As a result, wrinkles were formed across the flakes due to strain built-up in the structure. (d) AFM line profile (indicated by the green dashed line) across the flake. The thickness of the flake increased from ~7.3 nm in the central unlithiated region to ~10.8 nm in the outer lithiated regions. (e) AFM line profile (indicated by the blue dashed line) across the wrinkles in the lithiated region. The height of these wrinkles ranged from 20 to 50 nm with an average of 36.7 nm.

started to turn dark brown in color from the edges after a few minutes. This color change gradually extended from the edges to the center of the flake with constant biasing at 1.1 V (Figure 2d) and finally covered up the entire MoS<sub>2</sub> nanosheet after 30 min (Figure 2e). Previous studies on bulk MoS<sub>2</sub> reported a similar plateau at ~1.1 V during Li intercalation and attributed it to a phase transition<sup>7,10,19,25</sup> from 2H to 1T MoS<sub>2</sub>. Our observation confirms that the MoS<sub>2</sub> flake undergoes a 2H (semiconducting) to 1T (metallic) phase transformation at ~1.1 V versus Li/Li<sup>+</sup> to accommodate more Li<sup>+</sup> ions in its interlayer spacing. In addition, the optical images demonstrate that Li<sup>+</sup> ions (as well as the accompanying phase transition) enter MoS<sub>2</sub> flake from the edges and gradually diffuse toward the center of the flake. We note that in Figure 2e, MoS<sub>2</sub> regions under the metal electrodes remained greenish yellow in color. This was probably because the metal electrodes blocked the entry of Li<sup>+</sup> ions from the edges and also acted as a clamp to prevent or slow down the phase transformation and the resulting volume expansion. We did not go below 1.0 V versus

Li/Li<sup>+</sup> in the measurements to avoid the irreversible conversion reactions that form polysulfides.

Figure 2f–i shows the delithiation process of the same MoS<sub>2</sub> flake as we gradually increased its potential from 1.1 to 3.2 V with respect to Li/Li<sup>+</sup>. We could clearly visualize Li<sup>+</sup> ions moving out from the MoS<sub>2</sub> flake edges, as MoS<sub>2</sub> changed back to its original color, starting from the center and finally spreading to the edges. After complete delithiation at 3.2 V for 20 min (in Figure 3i), we noticed that the bottom/thinner part of the flake completely returned to its original color before lithiation (Figure 2b), suggesting a fully reversible discharge/charge cycle with little structural changes in the thinner region. We note that this is most likely not “sample damage” in the sense of changes within the covalently bonded layers but rather changes in the spacing between layers. At the top/thicker part, the color appeared to be slightly reddish compared to the original yellow. We have observed that MoS<sub>2</sub> shows different color contrast at different thicknesses with all other factors (substrate, light intensity, exposure time, and lens aperture)



being the same. Our AFM measurements confirm that yellow MoS<sub>2</sub> are typically ~25–35 nm thick while red MoS<sub>2</sub> typically have a thickness of ~40–55 nm. This suggests that the color change in MoS<sub>2</sub> from yellow to red after one discharge/charge cycle was possibly due to an increase in MoS<sub>2</sub> interlayer spacing caused by intercalation. Our AFM measurements on chemically intercalated MoS<sub>2</sub> nanoflakes (Figure 4d) confirmed that an average of 50% increase in interlayer spacing is observed. Thus, while thinner MoS<sub>2</sub> might fully restore its structure upon Li intercalation (see Supporting Information Figure 4), thicker MoS<sub>2</sub> seems to be unable to fully recover from lithiation and tends suffer some structural changes due to the larger accumulated strain. This may explain why MoS<sub>2</sub> based energy storage device typically suffer significant capacity loss upon cycling, especially after the first few cycles.<sup>7,26,27</sup>

We further investigated to verify if cycling causes structural changes in MoS<sub>2</sub> and if the yellow-to-red color change was due to cycling induced defects. Figure 3a–h shows a series of optical images of the same MoS<sub>2</sub> flake taken before device encapsulation with no electrolyte (Figure 3a) and at different cycles (Figure 3b–h) of Li intercalation. When fully delithiated at 3.2 V versus Li/Li<sup>+</sup>, we noticed that more red “bruises” start to appear on the MoS<sub>2</sub> nanosheet after several discharge and charge cycles of the MoS<sub>2</sub>. After the first cycle, the top of the film showed a yellow-to-red color change most likely due to the structural changes to MoS<sub>2</sub> (an increase in interlayer spacing in this case) from the intercalation process. In subsequent cycles 2 and 3, more of these red spots showed up throughout the flake, suggesting accumulating changes in the MoS<sub>2</sub> structure upon repeated cycling.

Through the top transparent glass slide, we also performed in situ Raman spectroscopy of our MoS<sub>2</sub> flakes during Li intercalation. Figure 3i shows Raman spectra of MoS<sub>2</sub> corresponds to the cycling condition indicated in Figure 2b–h. The red spot in Figure 2b indicates where the laser spot (Horiba 633 nm He–Ne laser source) was during the measurement. Immediately after our device encapsulation and before any electrochemical intercalation, the Raman spectrum (black, top) was consistent with that of a few-layer 2H-MoS<sub>2</sub>, which has been well studied.<sup>28–30</sup> The E<sub>2g</sub><sup>1</sup> (in-plane optical vibration of the Mo–S bond) and A<sub>1g</sub> modes (out-of-plane optical vibration of S atoms) were located at ~382 and 408 cm<sup>−1</sup>, respectively. The inset illustrates the schematics of these two first-order Raman-active modes in 2H-MoS<sub>2</sub>.

As we began the Li intercalation process by gradually lowering the MoS<sub>2</sub> potential from 2.1 to 1.2 V versus Li/Li<sup>+</sup>, Raman signals showed almost no change because Li<sup>+</sup> ion concentration in MoS<sub>2</sub> is relatively low before the 2H to 1T transition at ~1.1 V (see Supporting Information Figures 1 and 3). When MoS<sub>2</sub> was fully lithiated and transformed to the 1T phase (Figure 2c,e,g), Raman spectra were significantly different. We observed peaks at ~150 and 200 cm<sup>−1</sup>, which usually indicate a 2H to 1T phase transformation in MoS<sub>2</sub>, as reported in previous studies of chemically intercalated MoS<sub>2</sub> films.<sup>10,16,29,31</sup> However, A<sub>1g</sub> peaks, which are typically still present in the chemically intercalated MoS<sub>2</sub> samples, showed significantly lower intensity during lithiation as evident in curves c,e,g in Figure 2i. Supporting Information Figure 3f shows how the A<sub>1g</sub> mode intensity gradually decreased during lithiation and then slowly restored to its original level during delithiation. Similar observations of the reduction and broadening of the A<sub>1g</sub> phonon were reported by Chakraborty et al.<sup>32</sup> in monolayer MoS<sub>2</sub> and Kiriya et al.<sup>33</sup> in few-layer MoS<sub>2</sub> at high

doping level, attributed to strong electron–phonon coupling of the A<sub>1g</sub> mode. We suspect that in an electrochemical intercalation process with enough supply of electrons, Li<sup>+</sup> ion concentrations in MoS<sub>2</sub> (theoretical maximum at Li<sub>x=1</sub>MoS<sub>2</sub>) could be significantly higher than that in a chemical intercalation process (2 h in 1.6 M *n*-butyl lithium solution at 300 K). Thus, the presence of these Li<sup>+</sup> ions may have suppressed the out-of-plane S atom vibrations that contribute to A<sub>1g</sub> mode (see Supporting Information Figure 5 for a comparison of Raman Spectra of MoS<sub>2</sub> during chemical and electrochemical intercalations). The E<sub>2g</sub><sup>1</sup> mode in curve b also became part of a broad peak with a large line width in all subsequent curves (c–h) after the first lithiation. This peak broadening is typically a sign of structural defects in the crystal structure, possibly due to the volume expansion in MoS<sub>2</sub> caused by lithiation in this case. That is why the line width of the E<sub>2g</sub><sup>1</sup> mode remained large even when Li<sup>+</sup> ion concentration was low and MoS<sub>2</sub> was delithiated (Figure 2d,f,h).

In order to further investigate structural defects and strain built-up in MoS<sub>2</sub> from Li intercalation, we carried out AFM measurements on lithiated MoS<sub>2</sub> flakes. Because both the electrolyte and Li pellets are extremely reactive in air, we cannot perform AFM directly on the electrochemically intercalated devices. Instead, we immersed MoS<sub>2</sub> samples in *n*-butyl lithium solutions and used chemical intercalation to lithiate the flakes (see Methods for more details). Figure 4a,b shows optical images of the same MoS<sub>2</sub> flake before and after chemical intercalations (2 h in *n*-butyl lithium solution). The AFM image of the flake after intercalation is shown in Figure 4c. It confirms our previous observation that Li ions entered the MoS<sub>2</sub> van der Waals gaps from the edges and diffused toward the center, as it was evident from the outer ring of the lithiated region in Figure 4b,c. The color change in lithiated MoS<sub>2</sub> were due to an enhancement in optical transmission upon lithiation, which we will discuss in more details in the next section.

The dashed line profile across the flake is illustrated in Figure 4d. The MoS<sub>2</sub> thickness increases from 7.3 (center, unlithiated region) to 10.8 nm due to volume expansion caused by Li intercalation. There is a slight gradient of thickness from the edge (thicker) to the center (thinner) of the flake in both directions, possibly indicating the gradient of Li ion concentrations in MoS<sub>2</sub> from the edge (high) to the center (low). Besides the height increase due to accommodation of Li ions in the interlayer gaps, we also notice significant wrinkle formation in the lithiated region, along the entry direction of the Li ions. Because the intercalation process exerts significant strain on the MoS<sub>2</sub> crystal structure, the material eventually relaxes through these wrinkle formations. Similar distortion and wrinkling has been observed in the past on sodiated (Na<sup>+</sup>) MoS<sub>2</sub> films.<sup>34,35</sup> The height of these wrinkles ranged from 20 to 50 nm with an average height of 36.7 nm for this 7.3 nm thick MoS<sub>2</sub> flake (Figure 4e). These irreversible wrinkles and strains in Li<sub>x</sub>MoS<sub>2</sub> are possible reasons for the broadening of E<sub>2g</sub><sup>1</sup> Raman mode after the first lithiation, and for the cycling capacity loss in MoS<sub>2</sub>. This is especially true because the intercalated Li ion concentrations are probably higher in the electrochemical intercalation process (at 1.1 V versus Li/Li<sup>+</sup>) than in a chemical intercalation process (2 h in 1.6 M *n*-butyl lithium solution at 300 K) and therefore would cause more strain and wrinkles.

From both electrochemical and chemical intercalations, we observed significant change in color contrast of MoS<sub>2</sub> upon lithiation. In order to further investigate the optical properties

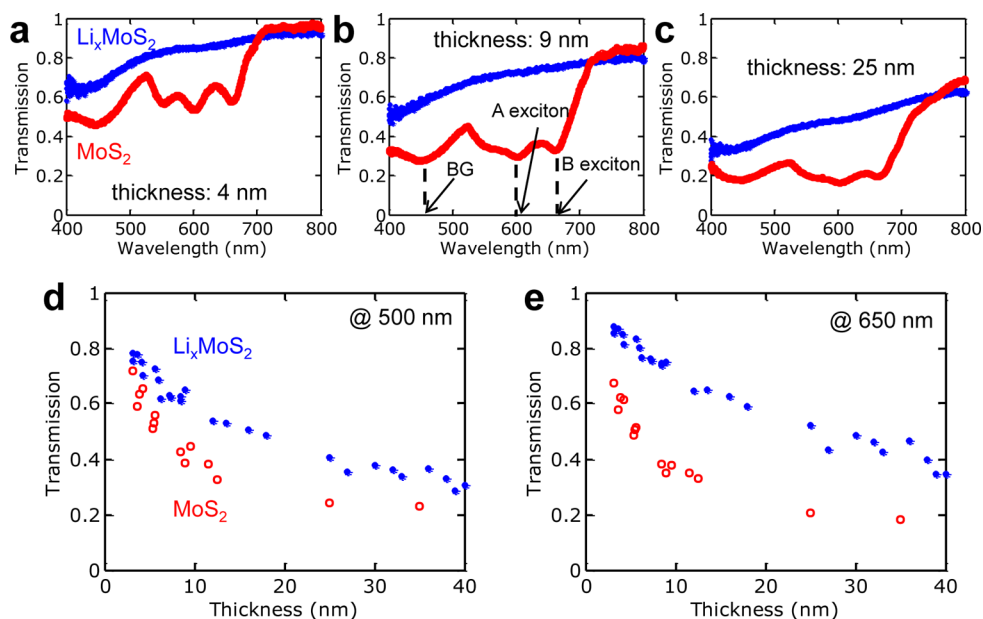


**Figure 5.** Optical characterizations of MoS<sub>2</sub> flakes upon Li intercalation. (a–c) Optical transmission spectra of MoS<sub>2</sub> flakes with various thicknesses (4, 9, and 25 nm) before (red) and after (blue) Li intercalations. (d,e) Thickness dependence of MoS<sub>2</sub> optical transmissions at 500 and 650 nm. The results showed enhancement in transmission after Li intercalation.

of MoS<sub>2</sub> upon Li intercalation, we performed spectral measurements (with a Nikon LV-UDM microscope) to characterize the optical transmission before and after Li intercalations. Here we exfoliated MoS<sub>2</sub> flakes onto quartz substrates and immersed them into 1.6 M *n*-butyl lithium solution for 2 h for chemical intercalation. The lateral dimensions of these MoS<sub>2</sub> flakes were typically 5–20  $\mu$ m, significantly larger than the spot size of the confocal microscope.

Figure 5a–c shows the transmission spectra of MoS<sub>2</sub> nanosheets before (red) and after (blue) 2 h of Li intercalation with initial thicknesses of 4, 9, and 25 nm, respectively. All optical transmission spectra were normalized to that of the quartz substrate that the sample sit on. We observe significant enhancement in transmission after Li intercalation at wavelengths between 400 and 700 nm, as well as slight decrease in transmission at wavelengths greater than 700 nm. This is consistent with recent observations by Wan et al.<sup>19</sup> For the 9 nm thick MoS<sub>2</sub> flake, the transmission in the visible range jumped from <30% in the pristine state to >70% after Li intercalation; while thin films (<5 nm) became highly transparent (>85%) after lithiation. Examining a larger range of thicknesses in Figure 5d,e, we also observe a clear dependence of optical transmission on the sample thickness. We plot the MoS<sub>2</sub> transmission before and after Li intercalation versus sample thickness at 500 and 650 nm wavelengths, respectively, in Figure 5d,e. Optical transmission enhancement after lithiation is observed in all thicknesses (measured by AFM) at both wavelengths.

We attribute at least part of the MoS<sub>2</sub> optical transmission enhancement between 400 and 700 nm to a substantial reduction in absorption after Li intercalation. There are three distinct local minima in the transmission spectrum of 2H-MoS<sub>2</sub> before intercalation (red curves in Figure 5a–c) at  $\sim$ 455 nm (2.73 eV), 603 nm (2.03 eV), and 660 nm (1.88 eV). These are due to absorption peaks at the corresponding energies. Previous studies of MoS<sub>2</sub> have also reported photoluminescence (PL)

bands at around 600 and 660 nm, which were attributed to band edge transitions in the K-point.<sup>36,37</sup> Figure 6a shows the schematic of the band structure of a few-layer thick 2H-MoS<sub>2</sub> flake at the K-point of the Brillouin zone. The A and B excitons are two exciton bands that are produced by band splitting at the K-point, possibly due to interlayer coupling.<sup>36–38</sup> The absorption peaks we obtained experimentally matched well with previously reported values. The high-energy absorption peak near 2.73 eV ( $\sim$ 455 nm) we observed is also consistent with recent optical measurements of MoS<sub>2</sub>.<sup>36,39,40</sup> While the origin of this high-energy exciton is still under debate, theoretical calculations suggest that this exciton may come from a background peak (BG) due to phonon–electron coupling<sup>36,39</sup> or a transition among the nesting bands between the  $\Gamma$  and  $\Lambda$  positions of the Brillouin zone.<sup>41</sup>

After Li intercalation, the 2H-MoS<sub>2</sub> undergoes a phase transformation to 1T-Li<sub>x</sub>MoS<sub>2</sub> lattice structure, which shows metallic behavior. Enyashin et al.<sup>42</sup> used density-function theory to calculate the band structure of 1T-Li<sub>x=1</sub>MoS<sub>2</sub>, where the valence and conduction bands were overlapped at the K-point (see schematic in Figure 6b), consistent with fully metallic behavior. Without the band gap, the absorption in 1T-Li<sub>x</sub>MoS<sub>2</sub> is substantially reduced, resulting in the optical transmission enhancement. We calculated the refractive indices of MoS<sub>2</sub> before and after Li intercalation (Figure 6c,d) from our thickness dependent transmission data (see Supporting Information). The imaginary parts of the MoS<sub>2</sub> refractive index became significantly less after Li intercalation, which is an indication of a decrease in light absorption of the material.<sup>20</sup>

Our electrochemical device also serves as a platform to allow in situ characterization and tuning of MoS<sub>2</sub> electrical transport properties. Four terminal MoS<sub>2</sub> devices were fabricated by e-beam lithography and e-beam evaporated Cr/Au contacts (Figure 1). As shown in Figure 7a, MoS<sub>2</sub> nanosheets demonstrated drastic improvement in electrical sheet resistance upon Li intercalation even down to a few nanometers in thickness. Four-probe measurements showed that lithiated

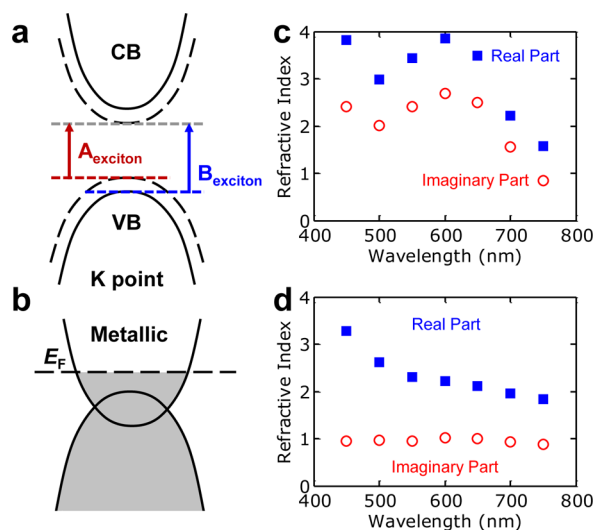


**Figure 6.** Reduction in absorption in MoS<sub>2</sub> after Li intercalation. (a) Schematic of the band structure of 2H-MoS<sub>2</sub> at the K-point in the Brillouin zone without Li intercalation. Optical transitions due to the A and B excitons are depicted. These transitions possibly cause absorption peaks in 2H-MoS<sub>2</sub>, which we observe as local optical transmission minima in Figure 5a–c. (b) Schematic of the band structure of 1T-Li<sub>x</sub>MoS<sub>2</sub> at the K-point in the Brillouin zone after Li intercalations. 1T-Li<sub>x</sub>MoS<sub>2</sub> shows a metallic behavior as the conduction band and the valence band becomes overlapped and the Fermi level lies in an incompletely filled band. This metallic band structure with no bandgap substantially reduces the light absorption. (c,d) The refractive indices of 2H-MoS<sub>2</sub> and 1T-Li<sub>x</sub>MoS<sub>2</sub>, respectively, as functions of wavelengths were calculated from the thickness dependent optical transmission measurements. The filled blue squares are the real part while the hollow red circles are the imaginary part of the refractive indices. In 2H-MoS<sub>2</sub>, higher values of the imaginary part at 450, 600, and 650 nm indicate higher absorption at these wavelengths, consistent with the transmission spectrum in Figure 5. In 1T-Li<sub>x</sub>MoS<sub>2</sub>, the imaginary part decreased significantly after Li intercalation, confirming a reduction in absorption due to the band structure change.

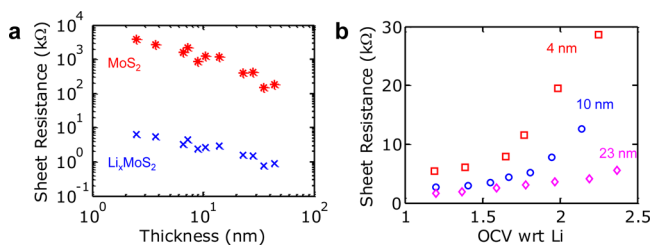


**Figure 7.** Electrical conductivity enhancement upon Li intercalation. (a) MoS<sub>2</sub> nanosheets with different thicknesses showed consistent decrease in sheet resistances by more than 100× after Li intercalation. (b) Sheet resistance of Li<sub>x</sub>MoS<sub>2</sub> (with thicknesses of 4, 10, and 23 nm) are plotted as a function of their potentials versus Li/Li<sup>+</sup>. This indicates that we could dynamically tune the Li<sub>x</sub>MoS<sub>2</sub> electrical conductivity by changing the Li<sup>+</sup> ion concentration in the interlayer gaps.

MoS<sub>2</sub> (biased at 1.2 V versus Li/Li<sup>+</sup>) typically exhibits over 2 orders of magnitude decrease in sheet resistance compared to pristine MoS<sub>2</sub>, due to the high carrier density and metallic behavior caused by Li intercalation. Together with the optical transmission enhancement, this improvement in electrical sheet resistance opens up new opportunities for applications in transparent electrodes. For example, a 4 nm thick MoS<sub>2</sub>

nanosheet exhibited optical transmission as high as 90% and showed more than 500× improvement in sheet resistance (from 2750 to 5.4 kΩ/sq.) upon Li intercalation. While this may be still short of the need for optoelectronic device applications (e.g., 90% and 10 Ω/sq. for ITO) at the moment, the large and tunable enhancement in both optical transmission and electrical conductivity through intercalation are promising and provides new opportunities in optoelectronics. Furthermore, our electrochemical platform enables dynamically tuning the MoS<sub>2</sub> sheet resistance in situ as a function of the Li ion concentration.

In Figure 7b, we plot the sheet resistance of Li<sub>x</sub>MoS<sub>2</sub> as a function of its relative potential with respect to Li/Li<sup>+</sup>. We observed that the Li<sub>x</sub>MoS<sub>2</sub> resistance decreased more than five times as we lowered the potential from ~2.3 to 1.2 V versus Li/Li<sup>+</sup>. This occurs because, as we vary the Li<sub>x</sub>MoS<sub>2</sub> potential against Li/Li<sup>+</sup>, we are tuning the Li concentration in Li<sub>x</sub>MoS<sub>2</sub> and therefore the carrier density and sheet resistance.<sup>10</sup> We can calculate exactly how the Li concentration in Li<sub>x</sub>MoS<sub>2</sub> changes as the potential in a bulk MoS<sub>2</sub> film, from a galvanostatic discharge curve of Li electrochemical intercalation into MoS<sub>2</sub> film (see Supporting Information Figure 1) and use that as a reference for our MoS<sub>2</sub> nanosheets. We did not lower the Li<sub>x</sub>MoS<sub>2</sub> voltage to less than 1.2 V versus Li/Li<sup>+</sup> in these measurements to avoid the volume expansion that may damage the electrodes or contacts. Our results suggest that Li intercalation significantly improve the MoS<sub>2</sub> optical transparency and electrical conductance. Similar effects have also been observed recently with Cu intercalation in Bi<sub>2</sub>Se<sub>3</sub><sup>20</sup> and Li intercalation in graphite,<sup>18</sup> making intercalation a potentially interesting technique for transparent electrode and touch screen applications.

The interlayer spacing in layered 2D materials accommodates the intercalation of large amounts of metal atoms. Our electrochemical platform enables direct observations of the reversible intercalation process in ultrathin nanosheets of 2D materials such as MoS<sub>2</sub>, and in situ characterization of their optical and electrical properties. We provide the first evidence of the dynamics of Li intercalation in nanoscale MoS<sub>2</sub> flakes. Through our optical, Raman and AFM measurements, we gain better understanding of the intercalation process and the possible structural changes in MoS<sub>2</sub> caused by repeated Li intercalation and deintercalation. These results provide possible explanations for cycling capacity loss in MoS<sub>2</sub> films and shed insights on improving performance of MoS<sub>2</sub>-based energy storage devices. Intercalation is also a powerful technique to dynamically tune the physical and chemical properties of material. Through Li intercalation, we achieve substantial improvement of MoS<sub>2</sub> optical transmission (up to 90% for a 4 nm flake) as well as more than 2 orders of magnitude increase in electrical conductivity for all flakes (~2–50 nm). Further investigations are under the way to study how intercalation could tune the thermal conductivity and Seebeck coefficient of Li<sub>x</sub>MoS<sub>2</sub>. The capability to reversibly engineer the physical and chemical properties of nanomaterials opens up exciting opportunities in optoelectronics, transparent electrodes, energy harvesting, and storage.

**Methods. Sample Fabrication.** Ultrathin MoS<sub>2</sub> flakes were exfoliated using the Scotch tape method onto a highly doped Si substrate with 90 nm of SiO<sub>2</sub> (Figure 1a). Inner electrodes (70 nm of Au) were patterned with e-beam lithography and deposited through e-beam evaporation (Figure 1b). Outer electrodes (1/70 nm of Cr/Au for MoS<sub>2</sub> and 50 nm of Cu for



Li pellet) were deposited through e-beam evaporation through a shadow mask (Figure 1c). The MoS<sub>2</sub> device was then transferred inside an Ar-filled glovebox, where a Li pellet is deposited onto the Cu electrode (isolated from MoS<sub>2</sub> electrodes). A cover glass (0.2 mm thick) was placed on top of the central region and epoxy was used to seal three sides of the glass. Because of the finite thickness of the Li pellet, a small pocket was created and fully filled with electrolyte (LiPF<sub>6</sub> in EC/DEC w/w = 1:1). The last (and fourth) side of the cover glass was then sealed with epoxy to isolate the electrolyte and Li pellet from the surrounding to prevent oxidations (Figure 1d,e). Care was taken to minimize the formation of gas bubbles.

**Electrochemical Intercalation and Electrical Transport Measurements.** Electrochemical intercalation was performed with a Biologic SP-150 potentiostat. Constant voltage charge and discharge were used to lithiate and delithiate MoS<sub>2</sub> nanosheets for in situ optical, Raman, and electrical measurements. Additional details were provided in the Supporting Information. Electrical transport characteristics of MoS<sub>2</sub> were measured with four-probe structures using a Keithley 4200-SCS parameter analyzer.

**Chemical Intercalation.** Samples were immersed into 1.6 M *n*-butyl lithium (Fisher Scientific) for 2 h. This was done at room temperature in an Ar-filled glovebox. After intercalation, we gently washed these samples with anhydrous hexane to remove organic residues. Samples were then sealed in an Al pouch cell within the glovebox (to slow down the oxidation of Li<sub>x</sub>MoS<sub>2</sub> in air) and transferred out for further analysis (AFM, electrical, and optical measurements).

**Optical Transmission Measurements.** Light transmission spectra were performed by an inverted microscope (Nikon LV-UDM microscope). White light was collected by a 50× objective with a numerical aperture of 0.8 using bright field mode. Spectral range was 400–800 nm. The photodetector (Princeton Instruments Spectrometry CCD) was cooled down by liquid N<sub>2</sub> with exposure time of 2 s.

## ■ ASSOCIATED CONTENT

### Supporting Information

The Supporting Information is available free of charge on the ACS Publications website at DOI: 10.1021/acs.nanolett.5b02619.

Setup for in situ optical measurements, additional Raman analysis, more optical images, TEM images, additional optical transmission results, electrical data, and XPS analysis.

(PDF)

## ■ AUTHOR INFORMATION

### Corresponding Authors

\*E-mail: [epop@stanford.edu](mailto:epop@stanford.edu).

\*E-mail: [yicui@stanford.edu](mailto:yicui@stanford.edu).

### Author Contributions

F.X., E.P., and Y.C. conceived the project. F.X. and H.W. fabricated the samples. F.X. carried out the optical microscopy, Raman spectroscopy, electrical transport, and AFM measurements. X.L. and F.X. carried out optical transmission measurements and analysis. J.S. performed TEM measurements. F.X., E.P., and Y.C. cowrote the manuscript. All authors discussed the results and commented on the manuscript.

### Notes

The authors declare no competing financial interest.

## ■ ACKNOWLEDGMENTS

This work is supported partly by the Stanford Nano- and Quantum Science and Engineering Postdoctoral Fellowship, the Army Research Office (ARO) Grant W911NF-13-1-0471, the Air Force Office of Scientific Research (AFOSR) Grant FA9550-14-1-0251. Y.C., H.W., and J.S. are supported by the Department of Energy (DOE), Basic Energy Sciences (BES), Materials Sciences and Engineering Division, under Contract DE-AC02-76SF00515.

## ■ REFERENCES

- (1) Chhowalla, M.; Shin, H. S.; Eda, G.; Li, L. J.; Loh, K. P.; Zhang, H. *Nat. Chem.* **2013**, *5* (4), 263–275.
- (2) Wang, Q. H.; Kalantar-Zadeh, K.; Kis, A.; Coleman, J. N.; Strano, M. S. *Nat. Nanotechnol.* **2012**, *7* (11), 699–712.
- (3) Butler, S. Z.; Hollen, S. M.; Cao, L. Y.; Cui, Y.; Gupta, J. A.; Gutierrez, H. R.; Heinz, T. F.; Hong, S. S.; Huang, J. X.; Ismach, A. F.; Johnston-Halperin, E.; Kuno, M.; Plashnitsa, V. V.; Robinson, R. D.; Ruoff, R. S.; Salahuddin, S.; Shan, J.; Shi, L.; Spencer, M. G.; Terrones, M.; Windl, W.; Goldberger, J. E. *ACS Nano* **2013**, *7* (4), 2898–2926.
- (4) Wang, H. T.; Yuan, H. T.; Hong, S. S.; Li, Y. B.; Cui, Y. *Chem. Soc. Rev.* **2015**, *44* (9), 2664–2680.
- (5) Radisavljevic, B.; Radenovic, A.; Brivio, J.; Giacometti, V.; Kis, A. *Nat. Nanotechnol.* **2011**, *6* (3), 147–150.
- (6) Wu, S.; Buckley, S.; Schaibley, J. R.; Feng, L.; Yan, J.; Mandrus, D. G.; Hatami, F.; Yao, W.; Vuckovic, J.; Majumdar, A.; Xu, X. *Nature* **2015**, *520* (7545), 69–72.
- (7) Xiao, J.; Choi, D. W.; Cosimbescu, L.; Koech, P.; Liu, J.; Lemmon, J. P. *Chem. Mater.* **2010**, *22* (16), 4522–4524.
- (8) Wu, J.; Schmidt, H.; Amara, K. K.; Xu, X. F.; Eda, G.; Ozyilmaz, B. *Nano Lett.* **2014**, *14* (5), 2730–2734.
- (9) Lee, G. H.; Yu, Y. J.; Cui, X.; Petrone, N.; Lee, C. H.; Choi, M. S.; Lee, D. Y.; Lee, C.; Yoo, W. J.; Watanabe, K.; Taniguchi, T.; Nuckolls, C.; Kim, P.; Hone, J. *ACS Nano* **2013**, *7* (9), 7931–7936.
- (10) Wang, H. T.; Lu, Z. Y.; Kong, D. S.; Sun, J.; Hymel, T. M.; Cui, Y. *ACS Nano* **2014**, *8* (5), 4940–4947.
- (11) David, L.; Bhandavat, R.; Singh, G. *ACS Nano* **2014**, *8* (2), 1759–1770.
- (12) Tan, C. L.; Zeng, Z. Y.; Huang, X.; Rui, X. H.; Wu, X. J.; Li, B.; Luo, Z. M.; Chen, J. Z.; Chen, B.; Yan, Q. Y.; Zhang, H. *Angew. Chem., Int. Ed.* **2015**, *54* (6), 1841–1845.
- (13) Wang, H. T.; Lu, Z. Y.; Xu, S. C.; Kong, D. S.; Cha, J. J.; Zheng, G. Y.; Hsu, P. C.; Yan, K.; Bradshaw, D.; Prinz, F. B.; Cui, Y. *Proc. Natl. Acad. Sci. U. S. A.* **2013**, *110* (49), 19701–19706.
- (14) Wang, Z. J.; Cao, X. H.; Ping, J. F.; Wang, Y. X.; Lin, T. T.; Huang, X.; Ma, Q. L.; Wang, F. K.; He, C. B.; Zhang, H. *Nanoscale* **2015**, *7* (21), 9394–9398.
- (15) Py, M. A.; Haering, R. R. *Can. J. Phys.* **1983**, *61* (1), 76–84.
- (16) Eda, G.; Yamaguchi, H.; Voiry, D.; Fujita, T.; Chen, M. W.; Chhowalla, M. *Nano Lett.* **2011**, *11* (12), 5111–5116.
- (17) Wang, Y.; Ou, J. Z.; Balendhran, S.; Chrimes, A. F.; Mortazavi, M.; Yao, D. D.; Field, M. R.; Latham, K.; Bansal, V.; Friend, J. R.; Zhuiykov, S.; Medhekar, N. V.; Strano, M. S.; Kalantar-zadeh, K. *ACS Nano* **2013**, *7*, 10083–10093.
- (18) Bao, W. Z.; Wan, J. Y.; Han, X. G.; Cai, X. H.; Zhu, H. L.; Kim, D. H.; Ma, D. K.; Xu, Y. L.; Munday, J. N.; Drew, H. D.; Fuhrer, M. S.; Hu, L. B. *Nat. Commun.* **2014**, *5*, 4224.
- (19) Wan, J. Y.; Bao, W. Z.; Liu, Y.; Dai, J. Q.; Shen, F.; Zhou, L. H.; Cai, X. H.; Urban, D.; Li, Y. Y.; Jungjohann, K.; Fuhrer, M. S.; Hu, L. B. *Adv. Energy Mater.* **2015**, *5* (5), 1401742.
- (20) Yao, J.; Koski, K. J.; Luo, W. D.; Cha, J. J.; Hu, L. B.; Kong, D. S.; Narasimhan, V. K.; Huo, K. F.; Cui, Y. *Nat. Commun.* **2014**, *5*, 5670.
- (21) Kappera, R.; Voiry, D.; Yalcin, S. E.; Branch, B.; Gupta, G.; Mohite, A. D.; Chhowalla, M. *Nat. Mater.* **2014**, *13* (12), 1128–1134.
- (22) Cho, J.; Losego, M. D.; Zhang, H. G.; Kim, H.; Zuo, J. M.; Petrov, I.; Cahill, D. G.; Braun, P. V. *Nat. Commun.* **2014**, *5*, 4035.

- (23) Koski, K. J.; Cha, J. J.; Reed, B. W.; Wessells, C. D.; Kong, D. S.; Cui, Y. *J. Am. Chem. Soc.* **2012**, *134* (18), 7584–7587.
- (24) Motter, J. P.; Koski, K. J.; Cui, Y. *Chem. Mater.* **2014**, *26* (7), 2313–2317.
- (25) Zhou, X. S.; Wan, L. J.; Guo, Y. G. *Nanoscale* **2012**, *4* (19), 5868–5871.
- (26) Suzuki, S.; Miyayama, M. *J. Phys. Chem. B* **2006**, *110* (10), 4731–4734.
- (27) Chang, K.; Chen, W. X. *Chem. Commun.* **2011**, 47 (14), 4252–4254.
- (28) Lee, C.; Yan, H.; Brus, L. E.; Heinz, T. F.; Hone, J.; Ryu, S. *ACS Nano* **2010**, *4* (5), 2695–2700.
- (29) Sandoval, S. J.; Yang, D.; Frindt, R. F.; Irwin, J. C. *Phys. Rev. B: Condens. Matter Mater. Phys.* **1991**, *44* (8), 3955–3962.
- (30) Fan, J. H.; Gao, P.; Zhang, A. M.; Zhu, B. R.; Zeng, H. L.; Cui, X. D.; He, R.; Zhang, Q. M. *J. Appl. Phys.* **2014**, *115* (5), 053527.
- (31) Lukowski, M. A.; Daniel, A. S.; Meng, F.; Forticaux, A.; Li, L. S.; Jin, S. *J. Am. Chem. Soc.* **2013**, *135* (28), 10274–10277.
- (32) Chakraborty, B.; Bera, A.; Muthu, D. V. S.; Bhowmick, S.; Waghmare, U. V.; Sood, A. K. *Phys. Rev. B: Condens. Matter Mater. Phys.* **2012**, *85* (16), 161403.
- (33) Kiriya, D.; Tosun, M.; Zhao, P. D.; Kang, J. S.; Javey, A. *J. Am. Chem. Soc.* **2014**, *136* (22), 7853–7856.
- (34) Lacey, S. D.; Wan, J. Y.; Cresce, A. V.; Russell, S. M.; Dai, J. Q.; Bao, W. Z.; Xu, K.; Hu, L. B. *Nano Lett.* **2015**, *15* (2), 1018–1024.
- (35) Park, J.; Kim, J. S.; Park, J. W.; Nam, T. H.; Kim, K. W.; Ahn, J. H.; Wang, G.; Ahn, H. J. *Electrochim. Acta* **2013**, *92*, 427–432.
- (36) Dhakal, K. P.; Duong, D. L.; Lee, J.; Nam, H.; Kim, M.; Kan, M.; Lee, Y. H.; Kim, J. *Nanoscale* **2014**, *6* (21), 13028–13035.
- (37) Mak, K. F.; Lee, C.; Hone, J.; Shan, J.; Heinz, T. F. *Phys. Rev. Lett.* **2010**, *105* (13), 136805.
- (38) Splendiani, A.; Sun, L.; Zhang, Y. B.; Li, T. S.; Kim, J.; Chim, C. Y.; Galli, G.; Wang, F. *Nano Lett.* **2010**, *10* (4), 1271–1275.
- (39) Qiu, D. Y.; da Jornada, F. H.; Louie, S. G. *Phys. Rev. Lett.* **2013**, *111* (21), 216805.
- (40) Molina-Sanchez, A.; Sangalli, D.; Hummer, K.; Marini, A.; Wirtz, L. *Phys. Rev. B: Condens. Matter Mater. Phys.* **2013**, *88* (4), 045412.
- (41) Carvalho, A.; Ribeiro, R. M.; Castro Neto, A. H. C. *Phys. Rev. B: Condens. Matter Mater. Phys.* **2013**, *88* (11), 115205.
- (42) Enyashin, A. N.; Seifert, G. *Comput. Theor. Chem.* **2012**, 999, 13–20.